Supplementary Materials for:

High Throughput Discovery of 2D Ferromagnetic and Multiferroic Transition Metal Oxyhalides and Nitrogen Halides

Shaowen Xu[1], Fanhao Jia[2ξ], Ning Dai[1 *]

[1]*School of Physics and Optoelectronic Engineering, Hangzhou Institute for Advanced Study, University of Chinese Academy of Science, Hangzhou 310024, China*

[2]*Department of Physics, College of Science, Hangzhou Dianzi University, Hangzhou 310018, P.R. China.*

[ξ] fanhaojia@shu.edu.cn; [*] ndai@mail.sitp.ac.cn

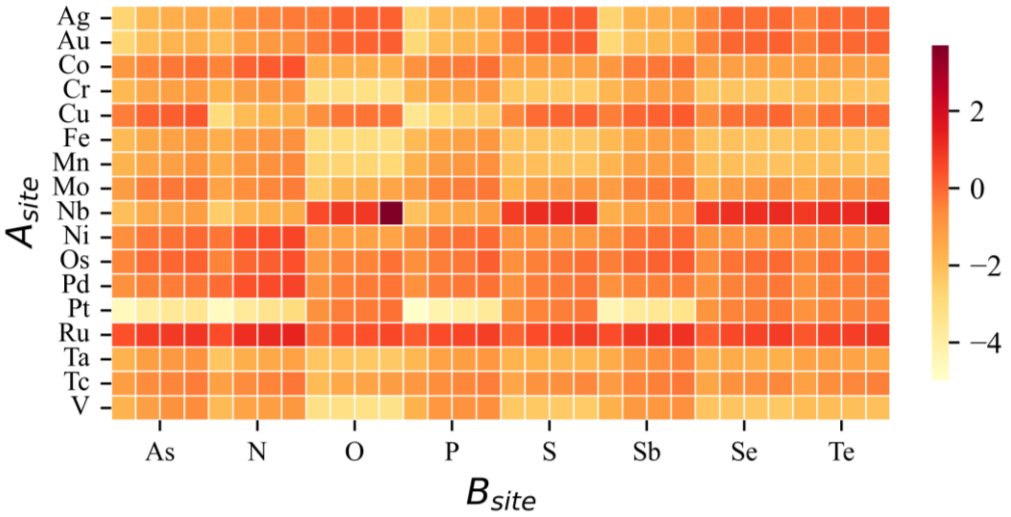

Figure S1. **Formation energy.** The formation energy is defined as: $E_f = \frac{E_{TMBC} - E_{TM} - E_B - E_X}{3}$, where E_{TMBX} is the total energy of monolayer T_MBX, and E_B and E_X are the average energies of the elements B and X in their stable crystal at 0 K.

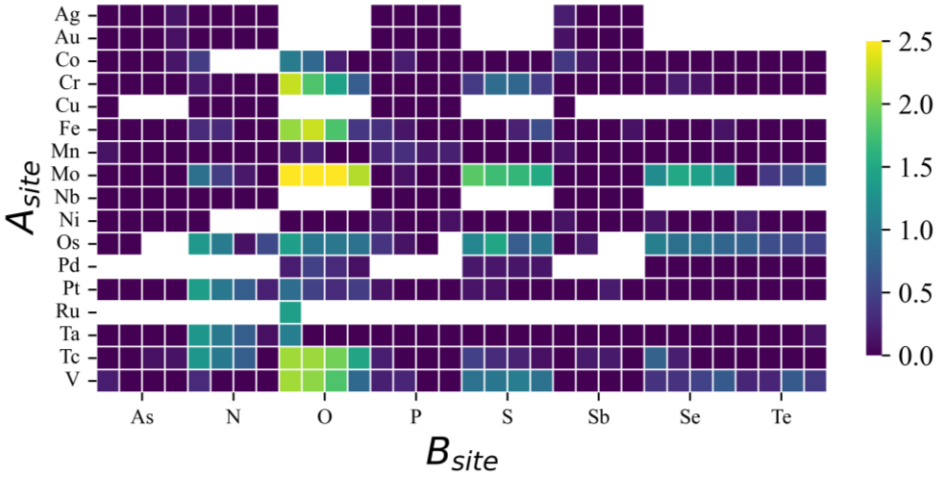

Figure S2. **Band gap.** The bandgap (eV) distribution of T_MBX monolayers calculated by PBE+U methods. The white squares represent unstable compounds.

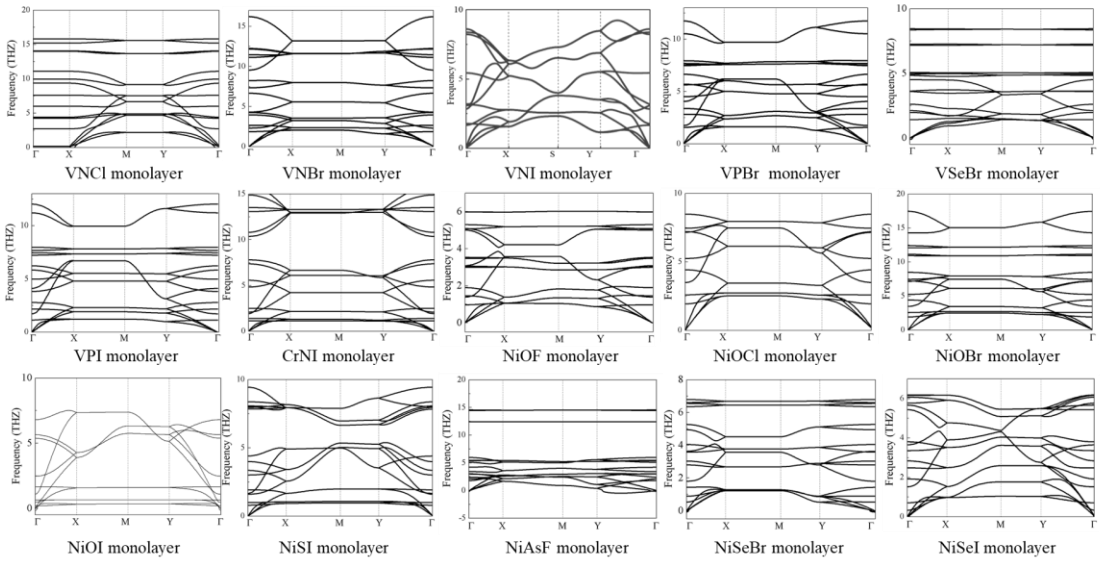

Figure S3. **Phonon dispersion of high-T_C T_MBXs.** The phonon dispersion of 15 high-T_C ($T_C \geq 400$ K) T_MBX monolayers.

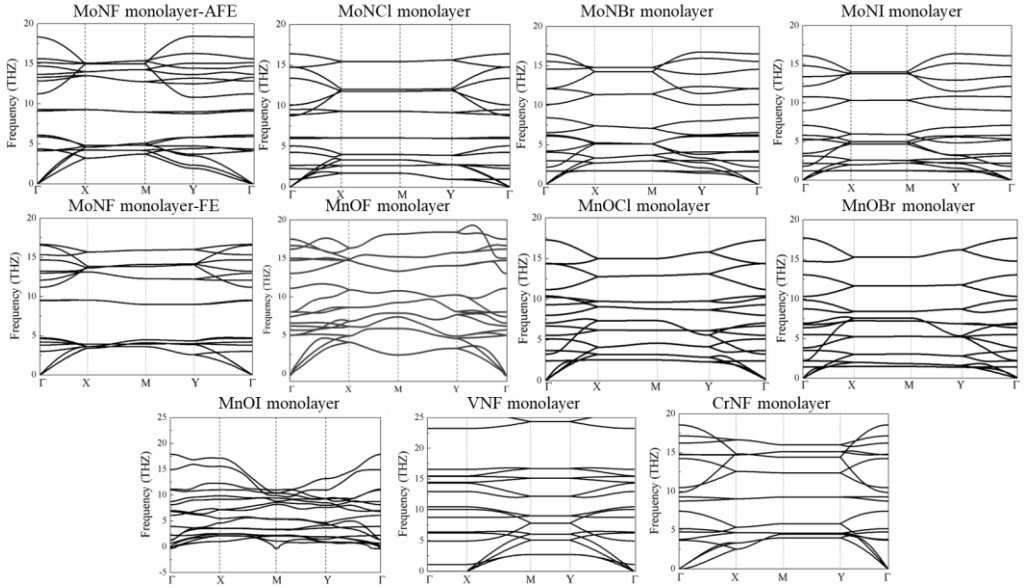

Figure S4. **Phonon dispersion of multiferroic T_MBXs.** The phonon dispersion of 11 high-T_C multiferroic T_MBX monolayers.

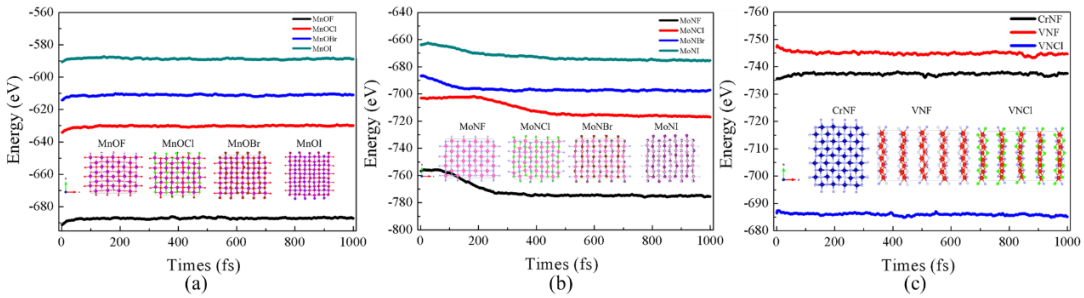

Figure S5. **Thermodynamic stability of multiferroic T_MBXs.** The thermodynamic stability of 11 high-T_C multiferroic T_MBX monolayers, confirmed by the *ab initio* molecular dynamics simulations.

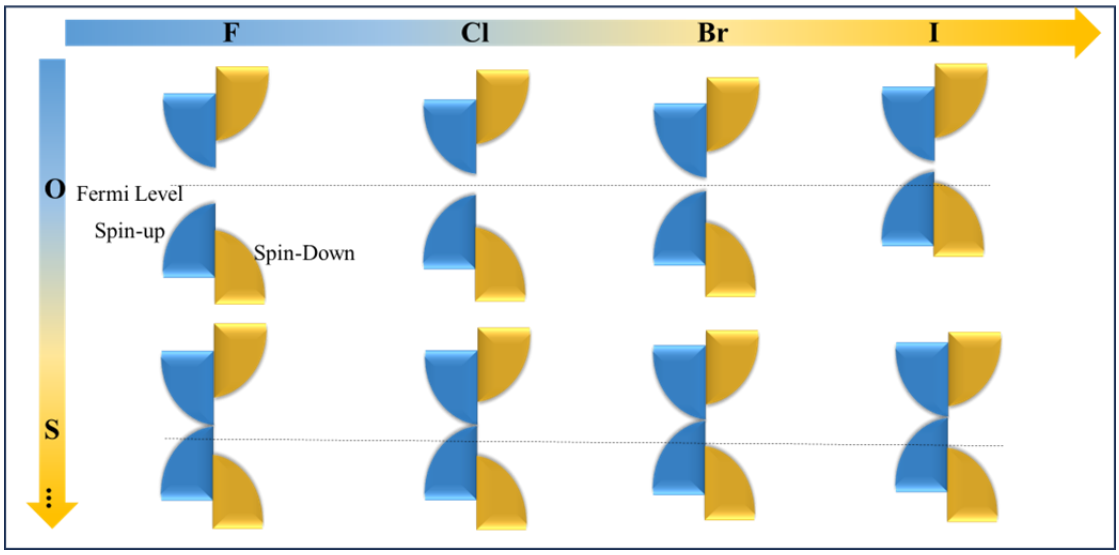

Figure S6. **Band alignment.** Schematic diagram for the band alignment of two spin channels as the varying of *B*- and *X*-sites elements.

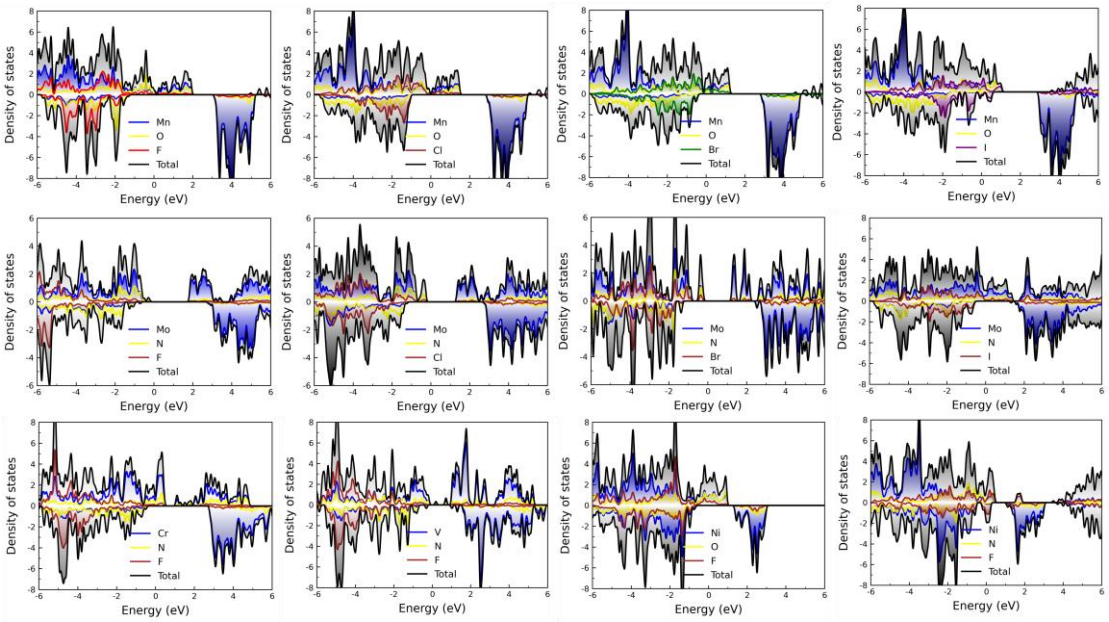

Figure S7. **Density of states.** The element-projected density of states for ferroelectric T_MBX monolayers.

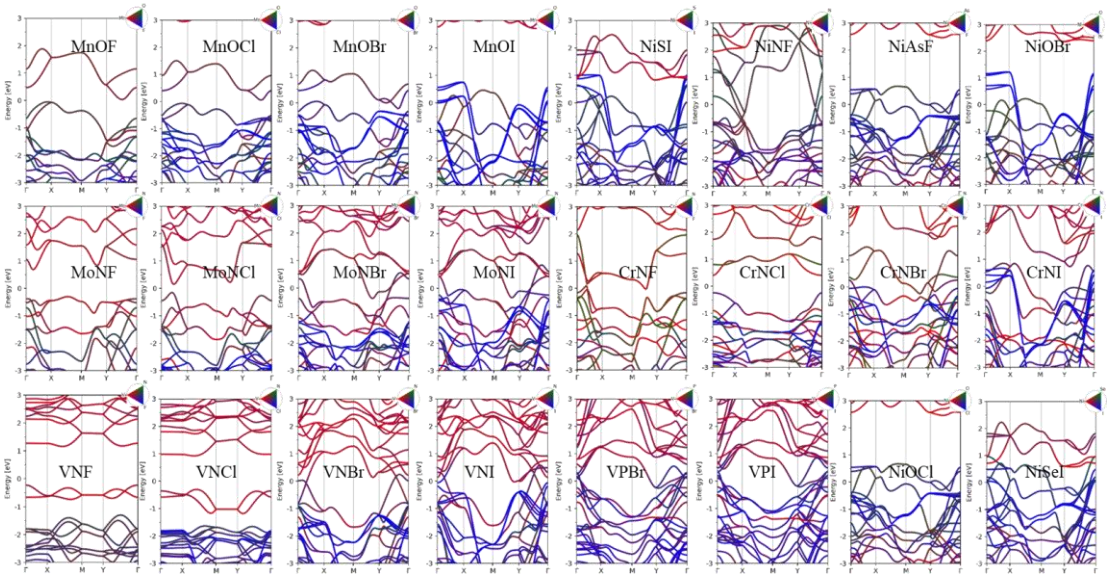

Figure S8. **Band structure.** The band structures of selected T_MBXs. Orange lines represent spin up, and blue lines is spin down. All band structures are calculated by PBE+U method.

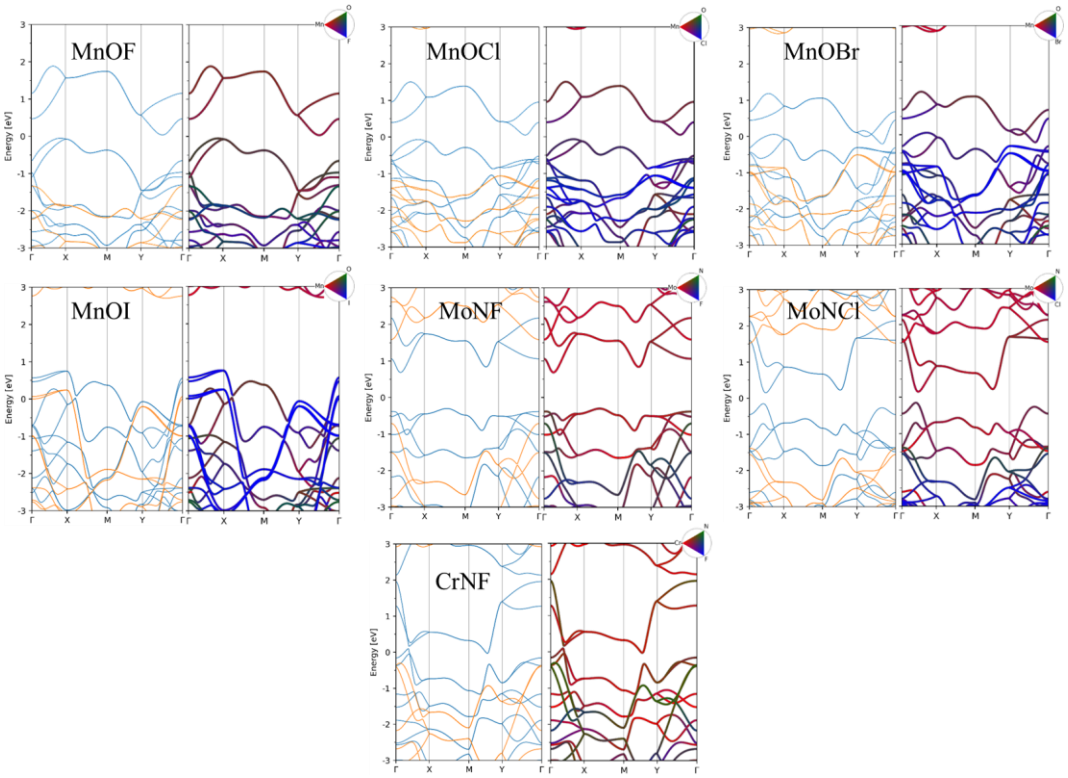

Figure S9. **Band structure of high-T_C multiferroic T_MBXs.** The band structures of 7 high-T_C multiferroic T_MBX monolayers. The blue and orange lines represent the spin-up and spin-down channels, respectively. The band structure with elemental projections of each system is also given.

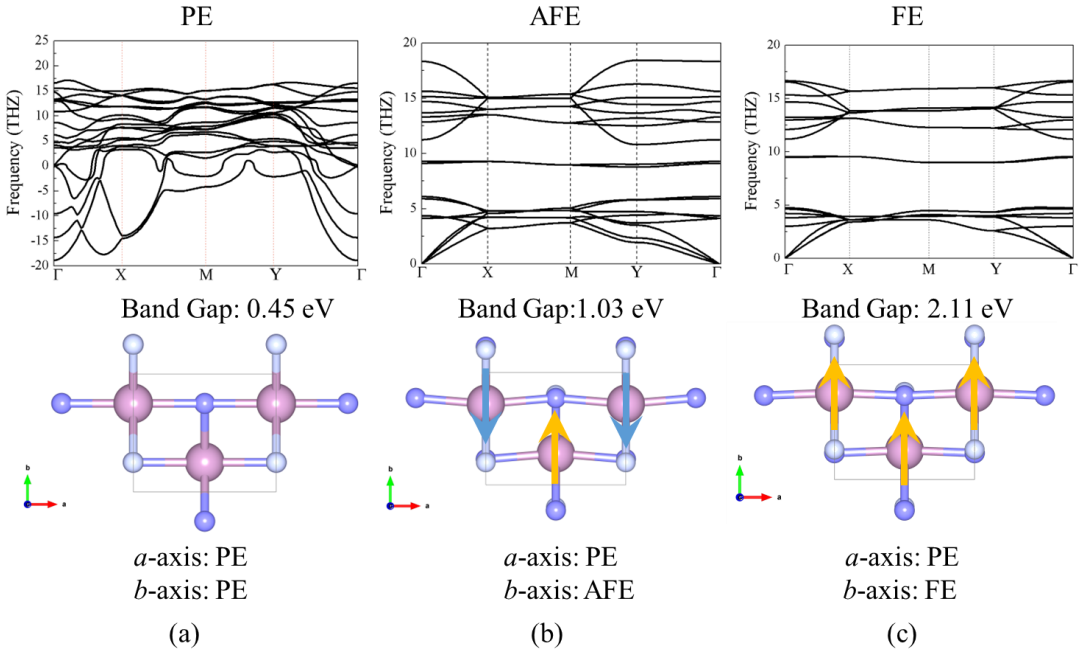

Figure S10. **Phonon spectra of MoNF monolayers.** (a) is the PE phase, (b) is AFE phase, and (c) is FE phase.

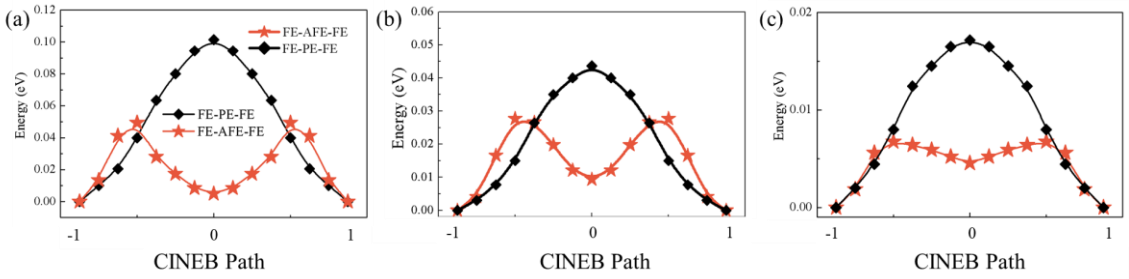

Figure S11. **Ferroelectric and antiferroelectric switching path.** The FE-AFE-FE and FE-PE-FE switching path of (a) MnOF monolayer, (b) MnOCl monolayer, and (c) MnOBr monolayer**.**

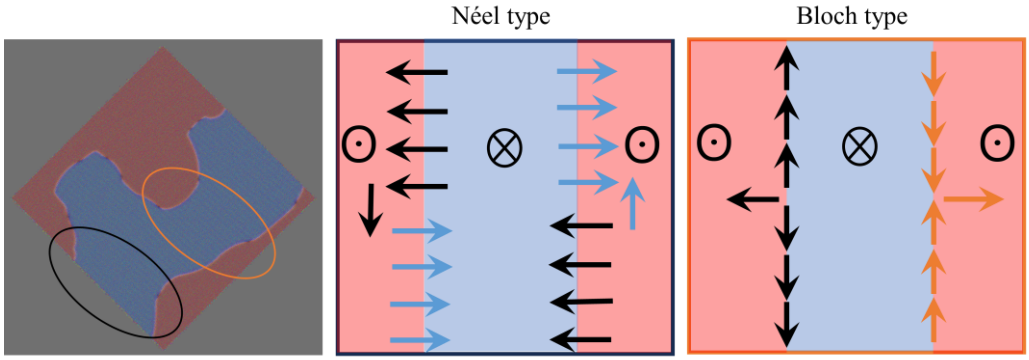

Figure S12. **Real-space spin textures.** Schematic diagrams of Neel and Bolch type spin textures. The left is Neel type, and the right is Bloch type.

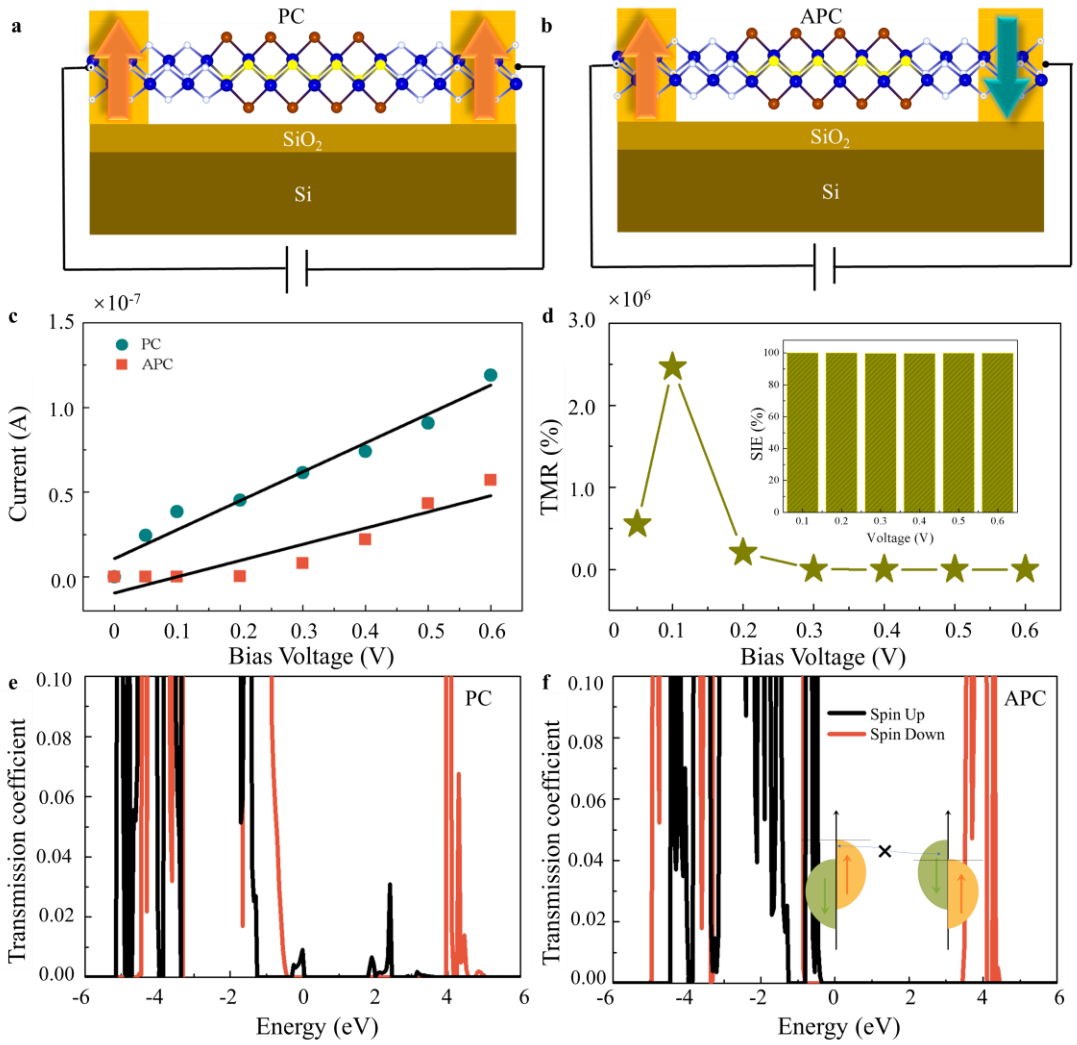

Figure S13. **Spin transport properties.** Schematic diagram of the CrNF/CrSBr/CrNF logic modulation with (a) parallel configuration (PC) and (b) antiparallel configuration (APC) states along *a*-axis. (c) I-*V* curve under PC and APC states. (d) TMR under different bias voltages. Inset is the SIE under different bias voltages. The transmission spectrum of CrSBr with (e) PC and (f) APC state simulated by PBE+*U* (*U* = 4 eV) method under equilibrium state.

Table S1. **The outermost electron arrangement of magnetic element**

Elements	Outermost electron configuration	Ions	Outermost electron configuration
V	$3d^3 4s^2$	V^{3+}	$3d^2\ (t_{2g})^2(e_g)^0$
Cr	$3d^5 4s^1$	Cr^{3+}	$3d^3\ \ (t_{2g})^3(e_g)^0$
Mn	$3d^5 4s^2$	Mn^{3+}	$3d^4\ (t_{2g})^3(e_g)^1$
Fe	$3d^6 4s^2$	Fe^{3+}	$3d^5\ (t_{2g})^3(e_g)^2/(t_{2g})^5(e_g)^0$
Co	$3d^7 4s^2$	Co^{3+}	$3d^6\ (t_{2g})^6(e_g)^0/(t_{2g})^4(e_g)^2$
Ni	$3d^8 4s^2/3d^9 4s^1$	Ni^{3+}	$3d^7\ (t_{2g})^6(e_g)^1/(t_{2g})^5(e_g)^2$
Mo	$4d^5 5s^1$	$Mo^{3+/4+}$	$4d^3\ (t_{2g})^2(e_g)^1/4d^2\ (t_{2g})^1(e_g)^1$
Tc	$4d^5 5s^2$	Tc^{3+}	$4d^4\ (t_{2g})^3(e_g)^1$

Table S2. **The magnetic parameter properties of 78 FM monolayers. The spin magnetic moment *S* (μ_B), magnetic exchange constant J_i (eV), magnetic anisotropy energies MAE (meV/T_M), magnetic easy axis (*L*) and T_C (K) of 78 FM**

	System	*S*	J_1	J_2	J_3	*MAE*	*L*	T_C
1	VSBr	2	0.0027	0.01071	0.004	0.00035779	*b*	120
2	VSeF	2	0.009	0.00205	0.006	0.00008326	*b*	140
3	VSeCl	2	0.009	0.002	0.003	0.00012326	*b*	130
4	VSeBr	2	0.022	0.004	0.018	0.00025600	*b*	400
5	VTeBr	2	0.019	0.0041	0.011	0.00001100	*b*	320
6	VNF	1	0.011	0.0447	0.006	0.00000900	*b*	380
7	VNCl	1	0.026	0.063	0.001	0.00001300	*b*	580
8	VNBr	1	0.011	0.0242	0.0059	0.00007850	*b*	600
9	VNI	1	0.04	0.03	0.025	0.00043610	*b*	650
10	VPBr	1	0.021	0.028	0.027	0.00048500	*c*	400
11	VPI	1	0.032	0.033	0.026	0.00107100	*b*	420
12	CrSF	3	0.013	0.0032	0.006	0.00002400	*c*	130
13	CrSCl	3	0.007	0.003	0.005	0.00002200	*b*	100
14	CrSBr	3	0.008	0.003	0.001	0.00011650	*b*	150
15	CrSI	3	0.00863	0.00292	0.00574	0.00108520	*c*	155
16	CrSeCl	3	0.014	0.0034	0.008	0.00019100	*b*	165
17	CrSeBr	3	0.013	0.00905	0.004	0.00048600	*b*	170
18	CrSeI	3	0.012	0.00965	0.003	0.00100540	*b*	180
19	CrTeCl	3	0.013	0.006	0.09	0.00256380	*c*	190
20	CrTeBr	3	0.015	0.002	0.011	0.00287580	*c*	195
21	CrTeI	3	0.01	0.0013	0.006	0.00234000	*c*	150
22	CrNF	2	0.009	0.01	0.005	0.00008460	*b*	300
23	CrNCl	2	0.021	0.009	0.0062	0.00006170	*a*	360
24	CrNBr	2	0.005	0.008	0.011	0.00090850	*a*	370
25	CrNI	2	0.016	0.0196	0.02	0.00148600	*c*	445

26	CrAsCl	3.76	0.00232	0.004	0.0023	0.00006400	*a*	80
27	CrAsBr	3.78	0.00382	0.00659	0.00306	0.00006360	*c*	111
28	CrAsI	3.78	0.00373	0.0067	0.00159	0.00112800	*c*	130
29	MnOF	4	0.003	0.0062	0.01	0.00011500	*c*	240
30	MnOCl	4	0.00545	0.0024	0.011	0.00006000	*c*	230
31	MnOBr	4	0.006	0.0045	0.012	0.00010020	*c*	220
32	MnOI	4	0.003	0.004	0.033	0.00044630	*b*	200
33	MnSF	4	0.0024	0.00476	0.02	0.00008070	*b*	220
34	MnSCl	4	0.003	0.00649	0.022	0.00007200	*b*	240
35	MnSBr	4	0.003	0.006	0.026	0.00044100	*b*	250
36	MnSI	4	0.003	0.00498	0.024	0.0010920	*b*	200
37	MnSeF	4	0.0046	0.00819	0.0031	0.00164600	*b*	110
38	MnSeCl	4	0.005	0.00905	0.0023	0.00247500	*b*	125
39	MnSeBr	4	0.001	0.00046	0.0007	0.0013530	*b*	80
40	MnAsBr	4.76	0.0007	0.00026	0.0009	0.00051500	*c*	40
41	MnSbBr	4.76	0.00147	0.00049	0.00051	0.00282200	*a*	60
42	MnSbI	4.78	0.00735	0.02383	0.00926	0.00232200	*a*	150
43	MnNF	3	0.00806	0.02518	0.00883	0.00004800	*c*	260
44	MnNCl	3	0.01022	0.03033	0.00875	0.00007900	*c*	273
45	MnNBr	3	0.00556	0.03834	0.00639	0.00042100	*b*	310
46	MnNI	3	0.014	0.0236	0.007	0.00275500	*b*	380
47	NiOF	1	0.027	0.114	0.039	0.00003660	*a*	675
48	NiOCl	1	0.028	0.141	0.01	0.00007570	*b*	620
49	NiOBr	1	0.013	0.152	0.078	0.00007830	*b*	610
50	NiOI	1	0.012	0.064	0.018	0.00053500	*c*	650
51	NiSI	1	0.10635	0.01942	0.03215	0.00177000	*b*	460
52	NiAsF	1	0.00329	0.04207	0.0732	0.00059360	*a*	490
53	NiSeBr	1	0.0288	0.03675	0.05513	0.00282596	*b*	680
54	NiSeI	1	0.00292	0.01729	0.09197	0.003662295	*b*	600
55	NiNF	1	0.0016	0.00881	0.01192	0.00005130	*b*	115
56	MoSBr	3	0.00217	0.01017	0.00466	0.00020550	*a*	110
57	MoSI	3	0.00116	0.00229	0.0152	0.00016400	*a*	105
58	MoSeF	3	0.00124	0.00485	0.01812	0.00020200	*c*	115
59	MoSeCl	3	0.00166	0.00644	0.01646	0.00011700	*b*	120
60	MoSeBr	3	0.00266	0.00941	0.00836	0.00007600	*a*	123
61	MoSeI	3	0.00176	0.00086	0.02011	0.00009500	*a*	95
62	MoTeF	3	0.00178	0.00243	0.01909	0.00031500	*b*	120
63	MoTeCl	3	0.00213	0.00288	0.01724	0.00045200	*b*	130
64	MoTeBr	3	0.00315	0.00628	0.01033	0.00024100	*b*	125
65	MoTeI	3	0.008	0.004	0.004	0.00021000	*b*	150
66	MoNF	2	0.013	0.028	0.022	0.00035000	*b*	420
67	MoNCl	2	0.011	0.015	0.00328	0.00048920	*a*	400
68	MoNBr	2	0.027	0.035	0.0178	0.00105540	*a*	560

69	MoNI	2	0.031	0.061	0.038	0.00104100	*a*	650
70	TcPCl	3	0.008	0.002	0.009	0.00017740	*a*	220
71	TcPBr	3	0.0038	0.0092	0.001	0.00052240	*a*	110
72	TcPI	3	0.00429	0.0096	0.00168	0.00068900	*a*	150
73	TcAsF	3	0.00595	0.0121	0.00445	0.00035400	*a*	170
74	TcAsCl	3	0.00499	0.01129	0.00266	0.00015700	*a*	156
75	TcAsBr	3	0.00452	0.01206	0.00112	0.00058530	*a*	123
76	TcAsI	3	0.00438	0.01254	0.00063	0.00091230	*c*	100
77	TcSbF	3	0.0019	0.01355	0.00148	0.00100800	*a*	150
78	TcSbCl	3	0.00047	0.00822	0.00121	0.00122540	*c*	40

Table S3. **The magnetic and electronic properties of 36 high-T_C FM semiconductors. Magnetism and electronic properties of 36 high-T_C FM semiconductors. The energy gap (eV) calculated by HSE06 method, the net magnetic moment per tradition metal atom M_{tot} (μ_B), and the Curie temperature (T_C, K)**

System	Gap	M_{tot}	T_C
VSeBr	0.76	2.0	400
VTeBr	0.00	2.0	320
VNF	2.15	1.0	380
VNCl	1.95	1.0	580
VNBr	HM	1.0	600
VNI	HM	1.0	650
VPBr	HM	1.0	420
VPI	HM	1.0	580
CrNF	0.36	2.0	300
CrNCl	0.24	2.0	360
CrNBr	0.20	2.0	370
CrNI	0.17	2.0	445
MnOF	1.58	4.0	240
MnOCl	1.35	4.0	230
MnOBr	0.80	4.0	220
MnOI	0.16	4.0	200
MnSF	HM	4.0	220
MnSCl	HM	4.0	240
MnSBr	HM	4.0	250
MnSI	HM	4.0	200
MnNF	0.20	3.0	250
MnNCl	0.31	3.0	260
MnNBr	0.39	3.0	273
MnNI	0.00	3.0	310
NiOF	0.00	1.0	675
NiOCl	0.00	1.0	620
NiOBr	0.00	1.0	610

NiOI	0.00	1.0	650
NiSI	0.00	1.0	460
NiAsF	0.00	1.0	490
NiSeBr	0.00	1.0	680
NiSeI	0.00	1.0	600
MoNF	0.80	3.0	420
MoNCl	0.66	3.0	400
MoNBr	0.23	3.0	560
MoNI	0.20	3.0	650

Table S4. **The Bader charge of T_M-site element in MnO*X* and CrN*X* systems.**

Bader charge of T_M	MnO*Xs*	CrN*Xs*
X = F	-1.73	-1.79
X = Cl	-1.59	-1.60
X = Br	-1.53	-1.54
X = I	-1.45	-1.49

Table S5. **The descriptions of the features.**

Descriptor	Unit
Boiling Point (BP)	℃
Mendeleev Number (MN)	/
Electron Affinity (EA)	kJ/mol
Bulk Density (BD)	/
Number of Valence Electrons (NVE)	/
Nearest-neighbor T_M-T_M distance (L_1)	Å
Next-nearest-neighbor T_M-T_M distance (L_2)	Å
Atomic Mass (AM)	/
Atomic Radius (AR)	/
Atomic Valency (AV)	/
Dipole Polarizability (DP)	/
Band Gap (E_g^{PBE})	eV
band gap (HSE)(Eg^{HSE})	eV
Fermi level (E_f)	eV
Magnetic Moment (M)	μ_B
Magnet Anisotropic Energy (MAE)	μeV/T_M
Nearest Neighbor Exchange Constant (J_1)	meV
Second Nearest Neighbor Exchange Constant (J_2)	meV
Third Nearest Neighbor Exchange Constant (J_3)	meV

Table S6. **Dzyaloshinskii-Moriya interaction parameters $D_{\parallel}$ and $D_{\perp}$ (meV) of FE and AFE MoNF monolayers.**

System	D_x	D_y	D_z
AFE	0.11	0.07	0.68
FE	0.43	0.29	0.68

Additional Computational details

2.1 *High-throughput and data screening*

We performed fully optimization calculations with FM and three antiferromagnetic (AFM) configurations by PBE+*U* method. A compound with negative formation energy (E_f) is required for synthesis. Here, we calculate the formation energy ($E_f = \frac{E_{TMBX} - E_{TM} - E_B - E_X}{3}$) to screen stable monolayer T_MBXs (**Figure** S1), where E_{TMBX} is the total energy, and E_B and E_X are the energies of the elements *B* and *X* in their stable crystal at 0 K. The effective Hubbard *U* parameter (U_{eff}) for V, Cr, Mn, Fe, Co, Ni and Mo are 3.3 eV, 3.7 eV, 4.0 eV, 5.3 eV, 4.0 eV, 6.2 eV, and 4.0 eV, respectively, which is consistent with the *U* values provided in the Materials Project.

2.2 *Magnetic exchange interactions*

The Monte-Carlo (MC) simulations are performed in *Vampire* program[1], an excellent computational tool based on anisotropic Heisenberg Spin Hamiltonian. The periodic boundary conditions were used to perform calculations. A large supercell 50 nm × 50 nm × 50 nm in our Monte-Carlo simulations is considered. Both equilibration and averaging phases are done using 50,000 steps. For each temperature step, 3×10^6 calculation steps were performed at a fixed time step of 0.1 fs.

For each T_MBXs, four likely magnetic orderings were generated, yielding a total of 308 FM and 924 AFM ground states. Magneto crystalline anisotropic energy (MAE) is calculated by using non-collinear DFT considered the spin-orbit coupling (SOC) effect in the next step. Finally, solving equations (1) yields the exchange parameters, J_i. For simplification, we only considered the nearest-neighbor (NN), next-nearest-neighbor (NNN) and third nearest neighbor (TNN) exchange interactions. The NN exchange coupling parameter is defined as J_1, the NNN exchange coupling parameter is J_2, and TNN exchange coupling parameter is J_3. In our T_MBX systems, magnetic ions are usually coupled indirectly through nonmagnetic atoms. There are three types of superexchange interactions: T_M-*X*-T_M (along *a*-axis direction with bond angle ~160°), T_M-*B*/*X*-T_M (along *b*-axis direction with bond angle ~95°), and T_M-*X*/*X*-T_M (along diagonal direction with bond angle ~95°). Usually, the superexchange interaction between magnetic-nonmagnetic-magnetic atoms with a bond angle of 180° is stronger than that with a bond angle of 90°. However, in our T_MBX systems, due the T_M-T_M distance along *a*-axis direction is much longer than that along *b*-axis direction, the T_M-*X*-T_M (bond angle ~160°) exchange coupling is weaker than T_M-*B*/*X*-T_M (bond angle ~95°). On the other hand, due to the electronegativity, the superexchange interaction of T_M-*B*-T_M is usually stronger than that of T_M-*X*-T_M, so the T_M-*B*/*X*-T_M exchange coupling (along *b*-axis direction with bond angle ~95°) is stronger than the T_M-*X*/*X*-T_M (along diagonal direction with bond angle ~95°) exchange coupling.

Since the bond length distributions of different T_MBX systems are different, there are three types of J_i configurations as indicated in Figure S14. Aomg these 78 FM T_MBXs, 22 systems are of type-1 configuration, 53 systems are of type-2 configuration, and 3 systems are of type-3 configuration. Here, the T_M-T_M distance along *a*-axis direction is colse to the diagonal T_M-T_M distance. For the majority (type-2 T_MBXs), J_2 coresponds to a diagonal T_M-*X*/*X*-T_M exhcnage coupling. Although the intensity of diagonal J_2 is weaker than the J_1 along *b*-axis, J_2 still plays a

more dominating role in determining T_C because J_2 interaction has four next-nearest neighbors, whereas J_1 interaction only has two nearest neighbors.

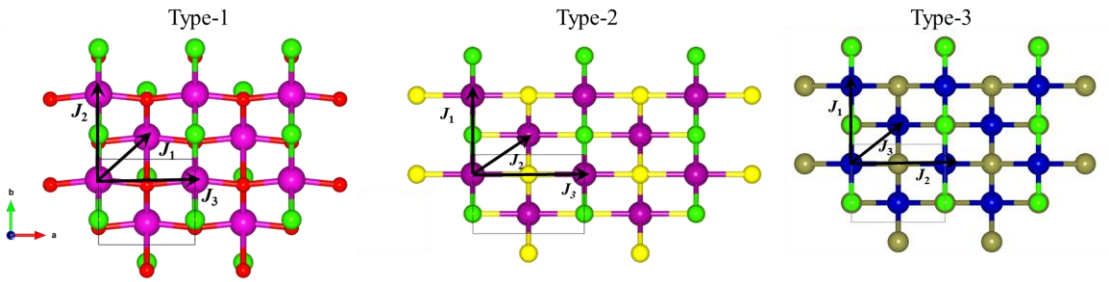

Figure S14. **The exchange coupling parameters of three types of T_MBX systems**. NN exchange coupling parameter J_1, NNN exchange coupling parameter J_2, and TNN exchange coupling parameter J_3.

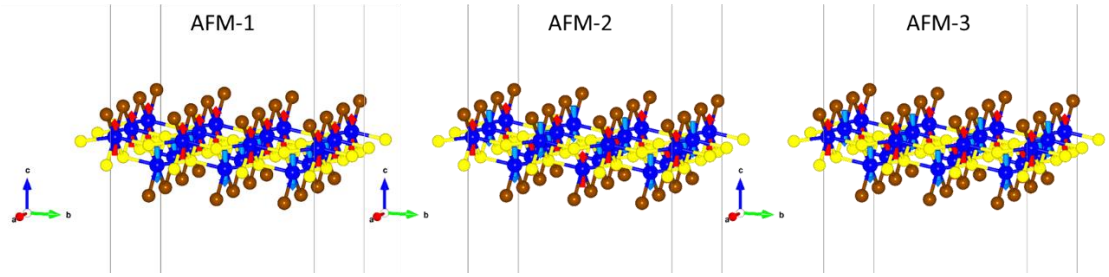

Figure S15. **The antiferromagnetic configurations of T_MBX monolayers**. It is used in the calculation of J_i, which are constructed by 3×3×1 supercells. The red and blue arrows represent the spin up and spin down, respectivly.

In T_MBX monolayers, magnetic exchange interactions between T_M atoms can be modeled considering up to third nearest-neighbors super exchange mechanisms through the *p* orbitals of *B* and *C* ligands. There are mainly three magnetic exchange interactions represented by J_1, J_2 and J_3, where J_1 accounts for the interaction between V-V atoms along the *a*-direction; J_2 coupling between V atoms from different "sublayers" along *c*; and J_3 the interaction between V atoms mediated by softer *B* atom bridges along the *b* axis.

The spin Hamiltonian based on the Heisenberg model is written as:

$$\mathbf{H} = -J_1 \sum_{\langle ij \rangle} \boldsymbol{S}_i \cdot \boldsymbol{S}_j - J_2 \sum_{\langle\langle ij \rangle\rangle} \boldsymbol{S}_i \cdot \boldsymbol{S}_j - J_3 \sum_{\langle\langle ij \rangle\rangle} \boldsymbol{S}_i \cdot \boldsymbol{S}_j - \boldsymbol{D} \sum_{\boldsymbol{i}} |\boldsymbol{S}_{\boldsymbol{i}}^{\boldsymbol{z}}|^{\mathbf{2}} \qquad (1)$$

where $\boldsymbol{S}$ is the spin magnetic moment of monolayer T_MBX, the anisotropy energy parameter $\boldsymbol{D}$ is defined as $\boldsymbol{D} = \frac{E_{hard}(axis) - E_{easy}(axis)}{|S|^2}$. A 50 × 50 ×1 square supercell (containing 2500 local magnetic moments) is adopted in the MC simulation.

Exchange coupling parameters J_1, J_2 and J_3 can be obtained from the energy differences between the FM and three AFM configurations, which can be calculated as the following equations of **Type-1**:

$$\frac{E_{FM}}{18} = E_0 - (4J_1 + 2J_2 + 2J_3)|S|^2 - D|S|^2 \qquad (2)$$

$$\frac{E_{AFM1}}{18} = E_0 - (-4J_1 + 2J_2 + 2J_3)|S|^2 - D|S|^2 \qquad (3)$$

$$\frac{E_{AFM2}}{18} = E_0 - (-2J_2)|S|^2 - D|S|^2 \quad (4)$$

$$\frac{E_{AFM3}}{18} = E_0 - (-4J_1 + 2J_2)|S|^2 - D|S|^2 \quad (5)$$

The exchange coupling parameters can be calculated as follows:

$$J_1 = \frac{E_{AFM1} - E_{FM}}{144|S|^2} \quad (6)$$

$$J_2 = \frac{E_{AFM2} - E_{AFM1}}{18|S|^2} + J_1 - \frac{J_3}{2} \quad (7)$$

$$J_3 = \frac{E_{AFM3} - E_{AFM1}}{36|S|^2} \quad (8)$$

Exchange coupling parameters J_1, J_2 and J_3 can be obtained from the energy differences between the FM and three AFM configurations, which can be calculated as the following equations of **Type-2**:

$$\frac{E_{FM}}{18} = E_0 - (2J_1 + 4J_2 + 2J_3)|S|^2 - D|S|^2 \quad (9)$$

$$\frac{E_{AFM1}}{18} = E_0 - (2J_1 - 4J_2 + 2J_3)|S|^2 - D|S|^2 \quad (10)$$

$$\frac{E_{AFM2}}{18} = E_0 - (-2J_1)|S|^2 - D|S|^2 \quad (11)$$

$$\frac{E_{AFM3}}{18} = E_0 - (2J_1 - 4J_2)|S|^2 - D|S|^2 \quad (12)$$

The exchange coupling parameters can be calculated as follows:

$$J_1 = \frac{E_{AFM2} - E_{AFM1}}{18|S|^2} + J_2 - \frac{J_3}{2} \quad (13)$$

$$J_2 = \frac{E_{AFM1} - E_{FM}}{144|S|^2} \quad (14)$$

$$J_3 = \frac{E_{AFM3} - E_{AFM1}}{36|S|^2} \quad (15)$$

Exchange coupling parameters J_1, J_2 and J_3 can be obtained from the energy differences between the FM and three AFM configurations, which can be calculated as the following equations of **Type-3**:

$$\frac{E_{FM}}{18} = E_0 - (2J_1 + 2J_2 + 4J_3)|S|^2 - D|S|^2 \quad (16)$$

$$\frac{E_{AFM1}}{18} = E_0 - (2J_1 + 2J_2 - 4J_3)|S|^2 - D|S|^2 \quad (17)$$

$$\frac{E_{AFM2}}{18} = E_0 - (-4J_3)|S|^2 - D|S|^2 \quad (18)$$

$$\frac{E_{AFM3}}{18} = E_0 - (2J_1 - 4J_3)|S|^2 - D|S|^2 \quad (19)$$

The exchange coupling parameters can be calculated as follows:

$$J_1 = \frac{E_{AFM2} - E_{AFM1}}{36|S|^2} - J_2 \quad (20)$$

$$J_2 = \frac{E_{AFM3} - E_{AFM1}}{36|S|^2} \quad (21)$$

$$J_3 = \frac{E_{AFM1} - E_{FM}}{144|S|^2} \quad (22)$$

2.3 *Quantum transport calculations using Nanodcal*

MnSBr-based spin transport simulations are implemented in the first-principles quantum transport package Nanodcal software,[2] which of the DFT is applied to the nonequilibrium Green's function (NEGF).[3] The exchange-correlation potential is explained by the Perdew-Burke-Ernzerhof (PBE) functional based on generalized gradient approximation (GGA). [4] *I-V* curve is obtained by calculating the current under different bias V_b, by Landauer-Buttiker formulation the current I under a specific bias voltage V_b can be obtained:[5]

$$I_\sigma(V) = e/h \int_{-\infty}^{+\infty} T(E, V_b)[f_L(E - \mu_L) - f_L(E - \mu_R)]\, dE \quad (23)$$

The spin-polarized thermal current relation with respect to temperature gradient is given by:

$$I\downarrow(\uparrow) = e/h \int_{-\infty}^{+\infty} [T(\downarrow) \uparrow (E)[f_L(E, T_L) - f_L(E, T_R)]\,]dE \quad (24)$$

Here, $T(\downarrow)\uparrow(E) = T_r(\Gamma_L\, G^R\, \Gamma_R\, G_A)(\downarrow)\uparrow$ represents the spin-polarized transmittance function. The temperature of the front and back FM layers are represented by T_F and T_B respectively. Equilibrium T_F and T_B Fermi-Dirac distribution function is represented by for right and left FM layers $f_{(F)}$ and $f_{(B)}$ respectively.

2.4 *Machine learning*

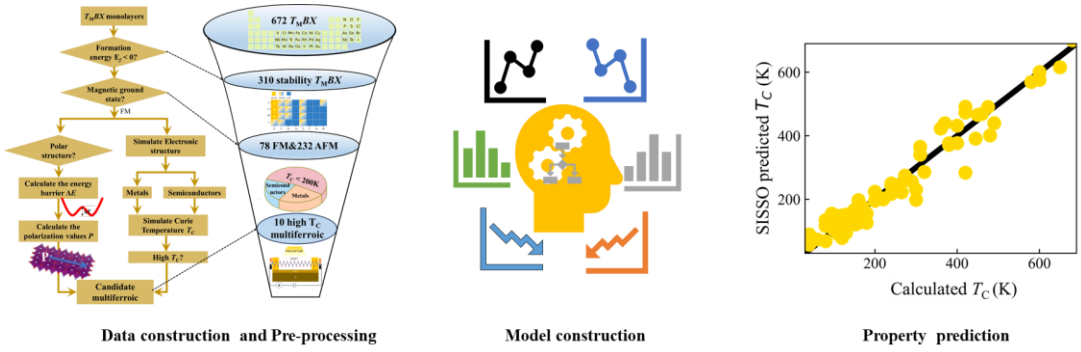

Figure S16. **The steps adopted for buliding machine learning model.** The flow inculdes data construction, model construction and properties predictions.

2.4.1 *Database Construction:*

Schematic representations of the steps adopted for building the supervised machine learning model are shown in Figure S16. The origin of our data source is from our first-principle high-throught data, which contains 310 stablity magnetic T_MBXs monolayers. Here, M refers to the transition-metal atom, and *B* stand for the O- and N-family, and *C* is the Halogen atoms (F-I). In

addition, the choice of descriptors is pivotal for the development of effective machine learning (ML) models. Our initial aim was to identify descriptors that are readily available, uniquely define the system, and forge a substantial connection with the target property.We utilize ML techniques to derive descriptors that can forecast the desired properties with minimal error. To be more precise, the principal descriptors under consideration are outlined in Table S5.

2.4.2 *Model construction*

Sure Independence Screening and Sparsifying Operator (SISSO) [6] is a data analysis method based on compressed sensing, which can identify an optimal low-dimensional feature descriptor from a large number of features. We use SISSO method to automatically constructs a feature space (Table S5) and subsequently selects the feature that better separates the classes in the training set.

Root mean square error is defined as: RMSE=$\sqrt{\frac{1}{n}\sum_{i=1}^{n}(p_i - e_i)}$, p_i and e_i are the predicted and experimental values of T_C, respectively, and n is the number of samples.

(1) 5D descriptor for predicting T_C:

$$\boldsymbol{D}_1 = J_3\text{-}J_1+\sqrt{J1 - M \times J1} \quad (25)$$

$$\boldsymbol{D}_2 = (J_2\text{-}J_3\text{-}J_3)\times(M\times |J1 - J2|) \quad (26)$$

$$\boldsymbol{D}_3 = \frac{J2sinM}{J1/M)-J3} \quad (27)$$

$$\boldsymbol{D}_4 = \frac{J1\times J3}{J3/J2)-cosM} \quad (28)$$

$$\boldsymbol{D}_5 = \left|sinM - \frac{J2}{J1}\times\sqrt{J2}\right| \quad (29)$$

Linear model using the SISSO descriptors:

$$T_C\ (\mathrm{K})=-0.12\times10^3+0.48\times10^4\times D_1+0.35\times10^5\times D_2-8.4\times D_3-0.34\times10^4\times D_4+0.62\times10^2\times D_5$$

(2) 4D descriptor for predicting J_2:

$$\boldsymbol{D}_1 = \mathrm{e}^{((\sin(M)\text{-}(\mathrm{EAX}^{\times}\mathrm{GAP})))} \quad (30)$$

$$\boldsymbol{D}_2 = \mathrm{IE}_B\times(\sin M + \sin\mathrm{Rad}_{TM}) \quad (31)$$

$$\boldsymbol{D}_3 = \mathrm{e}^{((\mathrm{L1}^{\times}\mathrm{L2})\text{ - }\frac{\mathrm{EAX}}{\mathrm{IE}B})} \quad (32)$$

$$\boldsymbol{D}_4 = \frac{M}{\mathrm{IE}B}\ |\ (M\text{-}\mathrm{L}_2)\ \text{-}\frac{\mathrm{EAX}}{\mathrm{Rad}TM}\ | \quad (33)$$

Linear model using the SISSO descriptors:

$$J_2\ (\mathrm{meV})=2.37+8.3\times D_1+0.75\times D_2+0.18\times10^6\times D_3-0.63\times D_4 \quad (34)$$

Reference:

[1] R. F. Evans, W. J. Fan, P. Chureemart, T. A. Ostler, M. O. Ellis, R. W. Chantrell, *Journal of Physics: Condensed Matter* **2014**, 26, 103202.

[2] S. Smidstrup, T. Markussen, P. Vancraeyveld, J. Wellendorff, J. Schneider, T. Gunst, B. Verstichel, D. Stradi, P. A. Khomyakov, U. G. Vej-Hansen, M.-E. Lee, S. T. Chill, F. Rasmussen, G. Penazzi, F. Corsetti, A. Ojanperä, K. Jensen, M. L. N. Palsgaard, U. Martinez, A. Blom, M. Brandbyge, K. Stokbro, *Journal of Physics: Condensed Matter* **2019**, 32, 015901.

[3] D. Stradi, U. Martinez, A. Blom, M. Brandbyge, K. Stokbro, *Physical Review B* **2016**, 93, 155302.

[4] a)P. Haas, F. Tran, P. Blaha, K. Schwarz, *Physical Review B* **2011**, 83, 205117; b)X. Li, H. Yu, F.

Lou, J. Feng, M.-H. Whangbo, H. Xiang, *Molecules* **2021**, 26, 803.

[5] H. M. Pastawski, *Physical Review B* **1992**, 46, 4053.

[6] R. Ouyang, S. Curtarolo, E. Ahmetcik, M. Scheffler, L. M. Ghiringhelli, *Physical Review Materials* **2018**, 2, 083802.